THE JOURNAL OF PHYSICAL CHEMISTRY C
A JOURNAL OF THE AMERICAN CHEMICAL SOCIETY

pubs.acs.org/JPCC

Article

Unraveling the Photophysics of Liquid-Phase Exfoliated Two-Dimensional ReS_2 Nanoflakes

Pieter Schiettecatte,[⊥] Deepika Poonia,[⊥] Ivo Tanghe, Sourav Maiti, Michele Failla, Sachin Kinge, Zeger Hens, Laurens D. A. Siebbeles, and Pieter Geiregat*

Cite This: *J. Phys. Chem. C* 2021, 125, 20993–21002

Read Online

ACCESS | Metrics & More | Article Recommendations | Supporting Information

ABSTRACT: Few-layered transition-metal dichalcogenides (TMDs) are increasingly popular materials for optoelectronics and catalysis. Among the various types of TMDs available today, rhenium chalcogenides (ReX_2) stand out due to their remarkable electronic structure, such as the occurrence of anisotropic excitons and potential direct band gap behavior throughout multilayered stacks. In this paper, we have analyzed the nature and dynamics of charge carriers in highly crystalline liquid-phase exfoliated ReS_2, using a unique combination of optical pump-THz probe and broad-band transient absorption spectroscopy. Two distinct time regimes are identified, both of which are dominated by unbound charge carriers despite the high exciton binding energy. In the first time regime, the unbound charge carriers cause an increase and a broadening of the exciton absorption band. In the second time regime, a peculiar narrowing of the excitonic absorption profile is observed, which we assign to the presence of built-in fields and/or charged defects. Our results pave the way to analyze spectrally complex transient absorption measurements on layered TMD materials and indicate the potential for ReS_2 to produce mobile free charge carriers, a feat relevant for photovoltaic applications.

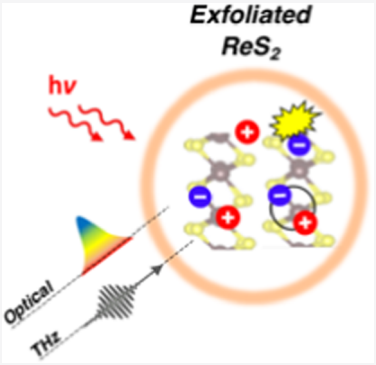

INTRODUCTION

Over the past few years, layered rhenium chalcogenide compounds have gained significant interest in the scientific community due to their anisotropic electronic and optoelectronic properties.[1] Rhenium disulfide (ReS_2) exhibits layer-independent optical properties due to electronically and vibrationally decoupled monolayers.[2,3] Among several implications, the possible preservation of a direct electronic band gap for thicker stacks sets ReS_2 apart from more conventional transition-metal dichalcogenides (TMDs), which suffer from indirect band gaps for multilayered stacks.[2,4−6] ReS_2 has shown great potential for transistors,[7−9] photodetectors,[10−12] light-emitting diodes,[13] and sensors.[14] Unlike conventional two-dimensional (2D) semiconductors, ReS_2 has a stable distorted 1T′ crystal structure and shows in-plane[15,16] and out-of-plane anisotropy.[17,18] This results in the formation of anisotropic excitons, and as a consequence, their fundamental properties, such as transport and[19] lifetimes, can be selectively modulated by varying the polarization of incident light.

Similar to other layered semiconductors, ReS_2 can be produced either through vacuum epitaxial growth, exfoliation from high-quality crystals, or direct colloidal synthesis.[20−23] Exfoliation, particularly through liquid-phase methods, is a cost-effective means to produce flakes of ReS_2 as it combines the advantages of solution processing (low cost and upscaling) while preserving high crystallinity, a persistent issue in direct colloidal synthesis methods.[24−26] An in-depth study of the synthesis of crystalline few-layered ReS_2 flakes through liquid-phase exfoliation has been reported recently, and first reports indicate their promising potential for PV applications.[27,28] Although high-quality ReS_2 nanoflakes obtained through such exfoliation procedures are clearly promising materials, the nature and dynamics of elementary optical excitations in these novel materials are not yet known, limiting their potential use in applications such as light emission or photovoltaics.

This contribution reports the temporal evolution of photogenerated excitons and free charge carriers in highly crystalline liquid-phase exfoliated 2D ReS_2 nanoflakes with few-monolayer thicknesses. To this end, we photoexcited the sample with ultrashort optical laser pulses and detected excitons and free charge carriers by both time-resolved optical probe and terahertz (THz) probe (conductivity) measurements.

EXPERIMENTAL SECTION

Liquid-Phase Exfoliation of ReS_2 and Film Preparation. Dispersions of ReS_2 were produced by liquid-phase exfoliation in *N*-methyl-2-pyrrolidone, as reported by us previously.[27] In brief, we mixed 50 mg of ReS_2 bulk powder

Received: June 15, 2021
Revised: September 9, 2021
Published: September 21, 2021

https://doi.org/10.1021/acs.jpcc.1c05268
J. Phys. Chem. C 2021, 125, 20993−21002

(≥99%, Alfa Aesar, 89 482.04) together with 25 mL of *N*-methyl-2-pyrrolidone (NMP, ≥99.0%, Merck) in a centrifugation tube. We sonicated the resulting mixture for a total duration of 6 h in a sonication bath (USC-THD, VWR) while keeping the bath temperature below 40 °C to avoid auto-oxidation of NMP.[29] Subsequently, we subjected the dispersion to centrifugation (Eppendorf model 5804, 30 min, 1700 rpm) to separate exfoliated flakes from unexfoliated material. The experimental parameters were optimized in our previous work. The supernatant that contains exfoliated ReS_2 flakes was decanted from the sediment and stored for further use. Such dispersions of ReS_2 in *N*-methyl-2-pyrrolidone were colloidally stable for months with limited sedimentation over time. Finally, a ReS_2 film, studied in this work, was prepared by drop-casting a ReS_2 dispersion on a quartz substrate, followed by annealing at 30 °C for 20 min.

Basic Characterization of ReS_2. For transmission electron microscopy (TEM), we diluted the dispersions of ReS_2 in isopropanol and cast a drop on a Holy Carbon−Cu grid (200 mesh, 50 μm). We removed traces of residual volatile components under a reduced atmosphere by drying samples in a vacuum tube connected to a Schlenk line or in the antechamber of a nitrogen-filled glove box. Low-resolution TEM images were taken on a Cs-corrected JEOL 2200-FS TEM at an acceleration voltage of 200 kV. In line with the literature, we prepared atomic force microscopy (AFM) specimens by casting a diluted ReS_2 dispersion in isopropanol onto a preheated silica wafer.[30] This method leads to isolated flakes onto a silica wafer with minimal contamination—conditions that are apt for height determination by AFM. Generally, we kept the specimens overnight in a vacuum tube connected to a Schlenk line or in the antechamber of a nitrogen-filled glove box before imaging the films on a Bruker dimension edge equipped with an NCHV probe using tapping mode in air. Following these methodologies, we expect minimal solvent remnants that could interfere with the height determination. Particle size distributions were measured by dynamic light scattering (DLS) on a Malvern Nano ZS Zetasizer equipped with a red He−Ne laser (λ = 633 nm). For X-ray photoelectron spectroscopy (XPS) and Raman spectroscopy, we cast a concentrated dispersion of ReS_2 in NMP on a microscopy glass slide and removed the solvent under vacuum in the antechamber of a glove box. XPS spectra were recorded on an S-Probe monochromatized XPS spectrometer using a monochromatized Al Kα source operated at 1486 eV as a probe. Raman measurements were conducted on a Bruker Optics Senterra dispersive Raman spectrometer attached to an Olympus BX51 microscope and coupled to a thermoelectrically cooled CCD detector, operating at −65 °C. The spectrometer has an XYZ motorized (automatic) stage for positioning and focusing. Spectra were obtained in the spectral range of 60−1560 cm^{-1} and with a spectral resolution of 3−5 cm^{-1} using a green Nd: YAG (532 nm) laser. The experimental conditions were set at five accumulations of 10 s, and sufficiently low laser power (0.1 mW) was used. All of the samples were measured under a ×50 magnification objective (numerical aperture (NA) of 0.75) with a spot size of 4 μm.

Transient Absorption (TA) Spectroscopy. TA measurements were performed by optically exciting and probing a ReS_2 film with ultrashort laser pulses, having a time duration of ≈180 fs, analogous to previous studies.[31−34] A Yb: KGW oscillator (Light conversion, Pharos SP) is used to produce 180 fs pulses with a 1028 nm wavelength at a 5 kHz frequency. The pump pulse is obtained by sending the fundamental beam through an optical parametric amplifier (OPA) equipped with a second harmonic module (Light conversion, Orpheus) to perform nonlinear mixing and achieve pump wavelengths of 310−1330 nm. The TA signal was detected using broad-band probe pulses generated in a sapphire (500−1600 nm) crystal. Pump and probe pulses overlap on the sample at a relatively small angle (∼8°), after which the pump pulses are dumped, and the probe light is collected at a detector. The pump-induced change in absorbance is calculated using

$$\Delta A = \log_{10}(I_{off}/I_{on})$$

where I is the incident light on the detector with either pump on or pump off. TA data is further corrected for probe-chirp using a polynomial function. In the present measurements, differential reflectance is not considered, and hence, differential transmittance is considered equal to differential absorbance. The pump photon fluence was determined using a thermopile sensor (Coherent, PS19Q). The ReS_2 film was stable during the laser spectroscopic measurements that were performed over a span of several months.

Optical Pump-THz Probe (OPTP) Spectroscopy. The terahertz conductivity setup is based on a laser system with a Mira Oscillator and a Legend HE-USP regenerative amplifier (by Coherent Inc). The measurements were performed by photoexciting a ReS_2 film with pump pulses of 60 fs duration and probing photogenerated charge carriers and/or excitons using single-cycle THz pulses which are generated in a nonlinear zinc telluride (ZnTe) crystal *via* optical rectification. The latter yields a THz waveform with a duration slightly longer than 1 ps, which determines the time resolution of the OPTP measurements.[35] The detection of the THz waveform takes place in a ZnTe crystal by spatially overlapping the THz pulse with a chirped optical laser pulse centered at 800 nm, such that the entire THz waveform is detected by a single laser shot, as explained in refs 36, 37. This method allows us to record the transmitted THz waveform before and after photoexcitation, *i.e.*, $E_0(t_p)$ and $E_{excited}(t_p, t)$ in a time window of about 3.5 ps, which is determined by the duration of the chirped optical pulse detecting the THz waveform. Here, the time t_p is the detection time of the THz probe waveform, and t is the time delay between the THz probe and the laser pump pulse that photoexcites the sample. After Fourier transformation of $E_0(t_p)$ and $E_{excited}(t_p, t)$ with respect to t_p we obtain the frequency-dependent change of the THz field as a function of the pump-probe time t; *i.e.*, $\Delta E(\nu, t) = E_0(\nu) - E_{excited}(\nu, t)$. The quantum yield weighted real and imaginary mobility of free charges and excitons is related to the differential THz signal $\Delta E(\nu, t)$ according to $S(\nu, t) = \frac{(1+n_s)c\varepsilon_0}{eN_a}\frac{\Delta E(\nu, t)}{E_0(\nu, t)}$, while n_s, c, ε_0, and e are the refractive index of the quartz substrate ($\sqrt{\varepsilon_s} = n_s = 2$), the speed of light in vacuum, the vacuum permittivity, and the elementary charge, respectively. N_a is the absorbed pump laser photon density per unit area.

RESULTS AND DISCUSSION

Linear and Transient Absorption Spectroscopy. Figure 1a (red trace) shows the linear optical absorbance spectrum of a ReS_2 film on quartz. The dashed black line indicates a fit with a polynomial background and an exciton

https://doi.org/10.1021/acs.jpcc.1c05268
J. Phys. Chem. C 2021, 125, 20993−21002

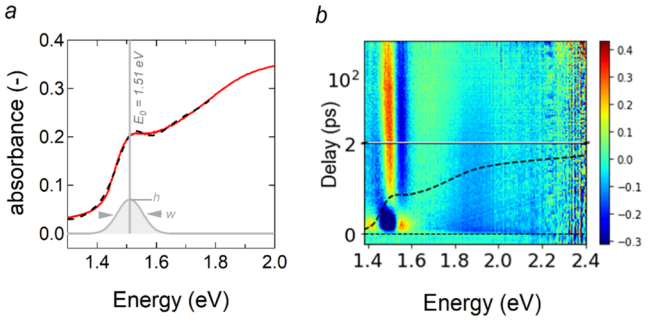

Figure 1. (a) Linear absorbance spectrum (red) of a thin film of ReS_2 nanoflakes obtained after drop-casting on quartz. The dashed black line reveals a fit of the absorbance spectrum, using a background with an exciton absorption profile centered at 1.51 eV (820 nm, gray shaded area) superimposed. The exciton profile is characterized by a width "w_0," an amplitude "h_0", and a central position $E_{X,0}$. (b) Overview of the transient absorbance ΔA recorded after a film of ReS_2 on quartz was photoexcited with a 180 fs pump pulse with photon energy 2.34 eV and absorbed photon fluence 1.2×10^{13} photons/cm^2 per pump pulse. The black dashed curve represents the linear absorbance spectrum.

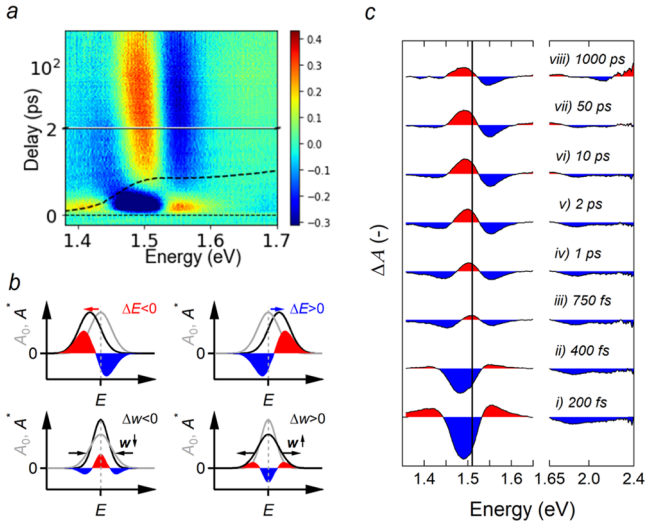

Figure 2. Overview of the transient absorbance ΔA spectroscopy in the band-gap region around 1.51 eV (820 nm). (a) Zoom of the 2D energy-delay map of ΔA under similar excitation conditions to Figure 1, showing a complex interplay between several spectral effects shown in (b). The black dashed curve again represents the linear absorbance spectrum. (b) Schematics of pump-induced effects on a Gaussian-shaped optical transition (from left to right and top to bottom): spectral redshift ($\Delta E < 0$), spectral blueshift ($\Delta E < 0$), linewidth narrowing ($\Delta w < 0$), and linewidth broadening ($\Delta w > 0$). (c) Transient absorbance spectra at time delays as indicated, plotted at an offset. For clarity, negative values of ΔA are filled in blue and positive values of ΔA are filled in red.

absorption profile centered at 1.51 eV (820 nm). We refer to the Experimental Section and Supporting Information Section S1 for an elaborate description of our liquid-phase exfoliation procedure and subsequent film preparation.[27]

The color map of Figure 1b provides a general overview of the transient absorbance (TA) spectroscopy data (see the Experimental Section) of such a ReS_2 film after photoexcitation with a 2.34 eV (530 nm) 180 fs pump pulse and interrogation by a broad-band probe spanning the energy range from 1.4 eV (880 nm) up to 2.4 eV (515 nm). The band-gap region shows a complex interplay of spectral effects, as shown in Figure 2a. We observe an interplay of different phenomena, such as exciton profile broadening or shifts, that can superimpose on a negative TA signal ($\Delta A < 0$) due to stimulated emission (SE) or bleach due to state-filling. A description of the effects of line shape shifts and broadening on ΔA spectra is provided in the Supporting Information S3, yet Figure 2b summarizes the main effects on a Gaussian transition line shape. To analyze the 2D TA map based on these qualitative concepts, we present spectral slices of ΔA at distinct pump-probe time delays in Figure 2c.

Immediately after photoexcitation (spectrum *i*, t = 200 fs), the spectrum exhibits a bleach ($\Delta A < 0$) around the exciton profile sided by two positive photo-induced absorptions (PA, $\Delta A > 0$). We recognize such a second-derivative-like line shape as a combination of SE and/or state-filling-induced bleach with a broadening of a Gaussian absorption profile; see Figure 2b ($\Delta w > 0$, bottom right) and the Supporting Information Section S3. The bleach minimum is slightly offset toward lower energy, and the PA band appears more intense at the higher-energy side. These asymmetries are likely the result of a blue-shifted exciton absorption line after the pump pulse, *i.e.*, a shift toward higher energy; see Figure 2b ($\Delta E > 0$, top right). At higher probe photon energy (>1.65 eV), the ΔA spectrum shows a net negative signal where the ground state absorbance A_0 has a relatively uniform slope up to 2.4 eV; see the dashed curve in Figures 1b and S2. Considering the extent of the negative band, it is unlikely to result from state-filling but presumably reflects a blueshift of the higher-lying energy states.

Most remarkably, while decaying, the signal at the band edge switches sign over the next few hundreds of femtoseconds (spectra ii–iv) and yields a clear photo-induced absorption sided by two bleach bands at a delay of 1 ps (spectrum iv). Such a feature reflects a narrowed exciton profile after photoexcitation of the sample, *i.e.*, the probe photon produces an exciton with a narrower linewidth than the exciton in the ground state absorption spectrum; see Figure 2b ($\Delta w < 0$, bottom left). At a delay of 750 fs (spectrum iii), the line shape is asymmetric, with a more intense negative tailing at a lower energy, *i.e.*, a shift to higher energy is superimposed on a narrowed exciton profile. At a delay of 1 ps (spectrum iv), the ΔA feature is symmetric, while at pump-probe delays longer than 1 ps (spectra v–vi), the symmetry is reversed, and the initial blueshift has decayed into a redshift; a process evidenced by a less intense tailing at lower energies and a shift of the PA maximum to the red side.

At higher energy (>1.65 eV), the blue-shifted continuum absorption has mostly decayed and even yields a slight redshift at decays longer than ≈10 ps (spectrum vi), a signature we recognize through the rise of a positive absorption band between 1.6–1.7 eV. In contrast, the signature at the band edge decays over a much longer timescale. While decaying (spectra vi–viii), the peak maximum in the ΔA progressively shifts to the lower energy and obtains a sinusoidal-like shape, which is characteristic of a spectral redshift of an absorption peak; see Figure 2b ($\Delta E < 0$, top left).

In summary, we recognize two dominant regimes in the ΔA map:

- Regime I, <3 ps: After photoexcitation, the exciton band broadens and blue-shifts. At the same time, we observe a blueshift of the higher-lying energy states.

https://doi.org/10.1021/acs.jpcc.1c05268
J. Phys. Chem. C 2021, 125, 20993–21002

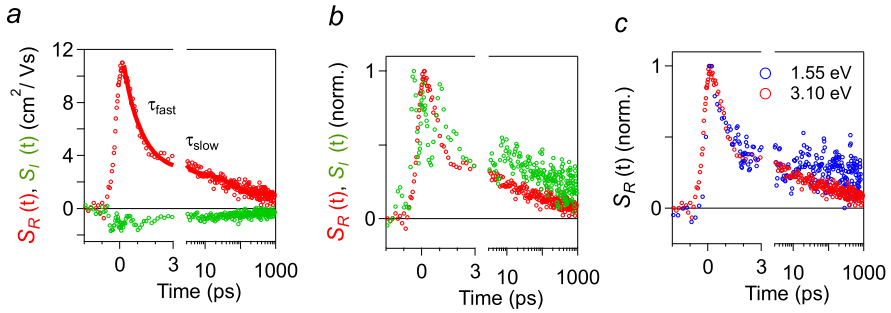

Figure 3. (a) Real and imaginary THz conductivity signal as a function of time obtained after photoexcitation with 3.1 eV energy and at an absorbed photon density N_a = 1.1 × 10^{13} cm^{-2}. The solid red curve is a biexponential fit revealing a fast and slow decay time constant; see also Figure 5. (b) Normalized kinetics of (a) to show the common decay channel for both real and imaginary parts of the conductivity. (c) Normalized kinetics of the real conductivity after photoexcitation with 1.55 eV (800 nm, red) pulses, resonant with the band gap, together with the off-resonant case (3.1 eV, blue) for a comparable absorbed photon flux.

- Regime II, >3 ps−1 ns: The initially broadened and blue-shifted exciton transition decays into its mirror image, *i.e.*, it narrows down and shifts to the red. At the same time, the blue-shifted higher-lying states gradually decay.

Optical Pump Terahertz Probe Spectroscopy. Having established two distinct regimes of TA dynamics in ReS_2, we now proceed to provide insights into the nature of photogenerated charges, albeit unbound carriers and/or excitons, that are present in each regime and how their presence could induce the observed spectral broadening and shifts in both regimes. The usually very large binding energy of excitons in 2D materials, *e.g.*, reported as 117 meV[38] for ReS_2, suggests the dominance of tightly bound excitons after energetic relaxation of initially unbound charge carriers produced by the pump laser pulse. However, trapping due to defects and binding energy reduction due to dielectric screening resulting from the presence of free or trapped charge carriers both result in a shift of the balance from excitons toward charge carriers.

To evaluate the presence and nature of photogenerated free charges versus excitons after photoexcitation, we first measured the differential transmission terahertz signal after photoexcitation at a pump photon energy of 3.1 eV (400 nm). Analogous to previous work, we consider the complex THz conductivity signal, $S(t)$, averaged over frequencies (ν) in the range of 0.6−1.1 THz, which is given by[37]

$$S(t) = \phi_{e,h}(t)\mu_{e,h} + \phi_{EX}(t)\mu_{EX} \quad (1)$$

where $\phi_{e,h}(t)$ is the time-dependent quantum yields of free mobile charges and $\mu_{e,h}$ is the sum of the complex-valued mobility of electrons and holes. The real and imaginary components of $\mu_{e,h}$ are due to the motion of charges with velocity in-phase and out-of-phase with respect to the THz field, respectively.[39,40] The second term in eq 1 takes into account the contribution of excitons with quantum yield ϕ_{EX} (t) and polarizability, α, which at a single radian frequency of the THz field (ω) is given by $\alpha = -eIm(\mu_{EX})/\omega$.[37]

The red curve in Figure 3a, due to the real THz conductivity signal from free charges, exhibits an initial fast decay over a timescale of *ca.* 3 ps at an absorbed photon density of 1.1 × 10^{13} photons/cm^2, which is comparable to the initial variation of the TA spectrum; see Figure 2a−c. Taking the initial measured value of $S_R(t)$ = 10 cm^2/V s (Figure 2a) and assuming the reported electron mobility values for bulk ReS_2 in the range 19−34 cm^2/Vs[41−43] to be comparable to the hole mobility,[41] we estimate the quantum yield of free pairs of electrons and holes to be in the range $\phi_{e,h}(t = 0) = 0.20 \pm 0.05$; see eq 1. After 3 ps, the remaining signal decays on a much longer timescale of several hundreds of picoseconds, possibly due to trapping of remaining charges.

The green curve in Figure 3a represents the imaginary component due to the motion of free charges with a velocity component that is out-of-phase with the applied THz field and/or the polarizability of free excitons.[37,39,40] However, we assert that the exciton polarizability is too small to contribute to the THz conductivity signal due to the experimental detection limit (see Supporting Information Section S4). Therefore, we attribute the observed small imaginary component to backscattering of free charges from randomly oriented stacks of ReS_2 flakes and possibly also from localized trap charges, as further discussed in Section S5 of the Supporting Information. When normalized and plotted together in Figure 3b, the real and imaginary THz conductivity signals follow the same decay kinetics, which strongly corroborates that the real and imaginary components originate from the same species; *i.e.*, unbound or "free" charges. When pumping at 800 nm (1.55 eV), no excess energy is provided to the charges, and excitons should be formed straight away. The THz transient overlays however perfectly with the 400 nm pump as is shown in Figure 3c. We hence conclude that a significant population of unbound charge carriers are present, in addition to weakly polarizable excitons, which will dominate the response of the nanoflakes.

By combining a qualitative assessment of the ΔA maps (Figure 2) and THz spectroscopy (Figure 3), we have identified two distinct time regimes of free or trapped charge carrier dynamics. To complete this analysis and compare THz to TA dynamics directly, we note that extracting reliable information from the complex and broad-band 2D TA map based on slices at fixed probe energies is prone to error. To better quantify the complex interplay of spectral effects that govern the free carrier-dominated TA response in the two time regimes, we proceed to fit $\Delta A(E, t)$ to a Gaussian fit function $G(h, E_{exciton}, w)$ that accounts for the exciton absorption and a background absorbance $C(E)$ attributed to higher-lying energy states (see Supporting Information Section S6). Using this procedure, we extract, for each pump-probe time delay the amplitude $h(t)$, the spectral position $E_{exciton}(t)$, and the width $w(t)$ of the Gaussian that describes the exciton band, similar to that in Figure 1a, and a shift of the background absorbance spectrum ΔE_{bck}. Next, we translate these into differential

https://doi.org/10.1021/acs.jpcc.1c05268
J. Phys. Chem. C 2021, 125, 20993−21002

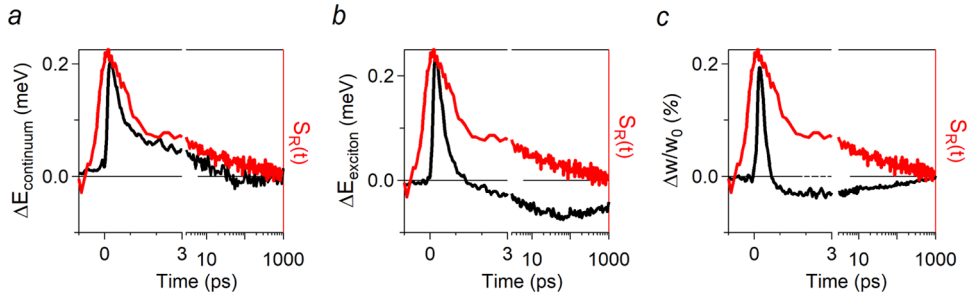

Figure 4. Evolution of the fit parameters (solid black lines) obtained from a fit of a Gaussian $G(h, E_{exciton}, w)$ with the constrained area and a background absorbance $C(E)$ to the ΔA in Figure 1b, including (a) the shift of the background absorbance ΔE_{bck} and, (b) the energy shift of the exciton $\Delta E_{exciton} = E_X(t) - E_{X,0}$, and (c) the normalized change in the width $\Delta w/w_0$.

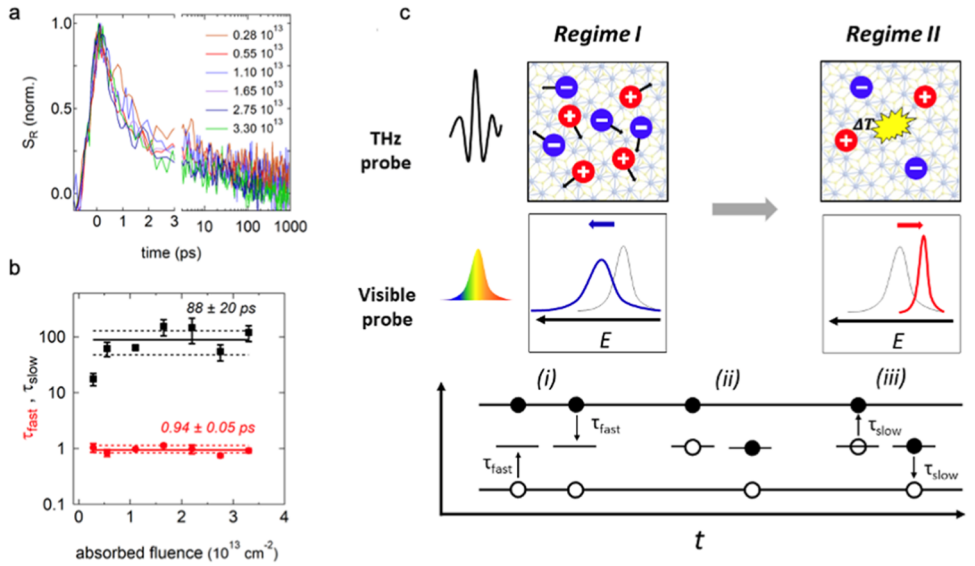

Figure 5. (a) Normalized decay traces of the real part of the THz conductivity, a metric for the charge population, for increasing absorbed photon density (0.28×10^{13}–3.3×10^{13} cm^{-2}). (b) Time constants extracted from a biexponential fit to (a) showing density-independent recombination dynamics for both fast (red, τ_{fast} = 0.94 ps) and slow (black, τ_{slow} = 88 ps) timescales. (c) Schematic summary representation of the proposed charge carrier generation and decay in liquid-phase exfoliated ReS_2, proceeding through two distinct regimes. An optical pump generates predominantly free mobile charge carriers, as evidenced by THz spectroscopy, that initially cause broadening and a blueshift of the exciton profile due to collisional broadening and free carrier screening, respectively. Next, the broadened and blue-shifted transition decays into a peculiar narrowed, and red-shifted line profile on a similar timescale as the THz conductivity decays. The latter indicates a nonradiative recombination event giving rise to the observed spectral signatures, *i.e.*, a redshift due to heating or carrier-capture-induced energetic redshifts and a narrowing due to a homogenization of the energy landscape.

quantities: $\Delta E_{exciton}$, Δw, and ΔE_{bck}. The results of this quantitative analysis of the ΔA maps, as summarized in Figure 4a–c, reproduce the qualitative assessment put forward earlier, *i.e.*, the complex spectral response is a result of an interplay between linewidth changes and spectral shifts and is split into two time regimes. Remarkably, the temporal evolution of the spectral parameters $\Delta E_{exciton}$, Δw, and ΔE_{bck} coincides quite well with the decay of the real component of the THz conductivity shown in Figure 3a and overlaid in Figure 4a–c (red curve). A single-exponential fit reveals time constants of 0.47 and 0.42 ps for $\Delta E_{exciton}$, and ΔE_{bck} respectively, and a 0.27 ps time constant for Δw. The slower rise and *ca.* 1 ps decay of the THz conductivity signal is due to the lower time resolution of OPTP measurements compared to TA spectroscopy; see the Experimental Section.

Carrier Dynamics. Remarkably, the decay of the carrier population is independent of carrier density, as is evidenced by the decay traces of the real THz conductivity in Figure 5a over an order of magnitude in pump fluence. A double-exponential fit to the full decay reveals two lifetimes: τ_{fast} = 0.94 ps and τ_{slow} = 88 ps; see Figure 5b. We use the fast component, which is limited by the OPTP time resolution, as a tentative ruler to set the regimes apart, *i.e.*, after three decay constants (*ca.* 3 ps), we assume the effects of regime I are finished. Such fluence independent behavior was also observed in flakes of other TMD materials and typically points toward fast trapping of one charge carrier, followed by nonradiative recombination through a Shockley–Read–Hall mechanism (Figure 5c, bottom).[24,25,44]

Regimes of Charge Recombination. Based on the acquired TA and THz data analysis, we outline two time regimes, both of which are dominated by free mobile charge carriers, which are discussed in detail below; see also Figure 5c.

Regime I (<3 ps): Linewidth Broadening and Blueshifts. The optical pump generates predominantly free charge carriers that initially broaden the exciton resonance due to collisional broadening and blue-shift the exciton energy due to a free carrier screening mechanism (Figure 4a). Collisional broad-

https://doi.org/10.1021/acs.jpcc.1c05268
J. Phys. Chem. C 2021, 125, 20993–21002

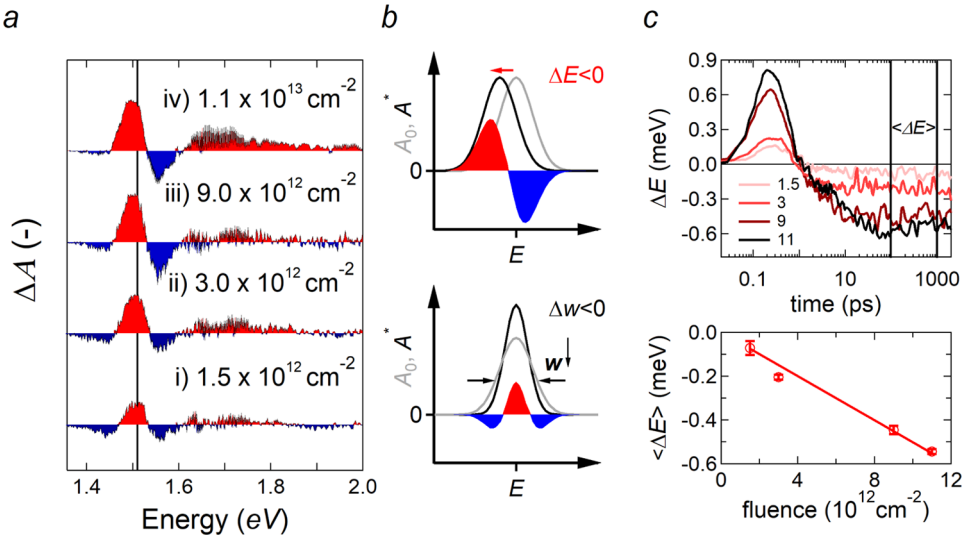

Figure 6. (a) Redshift of the exciton peak for increasing absorbed pump fluence at a probe delay time of 1 ns. (b) Schematics depicting how a redshift and line narrowing manifest in TA spectra. (c) (Top) Evolution of the energy shift of the exciton obtained from Gaussian fit with a constrained area and background absorbance to fluence-dependent ΔA maps for increasing densities of 1.5×10^{12}–11×10^{12} cm^{-2}. (Bottom) Averaged exciton energy shift $\langle \Delta E \rangle$, here averaged between 100 and 1000 ps (see also (c), top graph), as a function of fluence. Markers represent experimental data points, and the solid curve is a linear fit through the origin.

ening is responsible for broadening spectral lines in atoms and molecules and absorption and emission lines in semiconductors.[45−48] In addition to the broadening, we also observe a blueshift of the spectrum due to the screening of Coulomb forces, resulting in the reduction of the binding energy of excitons.[49] The central position of an exciton resonance E_X depends on the exciton binding energy, E_b, and the free-particle band gap, E_g, such that $E_X = E_g - E_b$.[50] It is well known that the presence of carriers alters the Coulomb potential experienced by electrons and holes. Screening of attractive electron−hole interactions decreases the exciton binding energy (binding energy reduction, BER), causing blueshifts, while electron−electron (exchange) interactions renormalize the band gap (band gap renormalization, BGR), causing redshifts.[51,52] Both mechanisms work in spectrally opposite directions yet do not fully compensate in general. As such, screening results in either a blueshift or a redshift of the exciton profile.[53] For instance, blue-shifted exciton transitions as a result of screening have been observed in quasi-2D QWs.[46,47,53,54] atomically thin TMDs,[48,49,55] and 2D layered perovskites.[56] In MoS_2[48] and WS_2,[49,55] blueshifts at early delays were always accompanied by a broadening, similar to our observations.

It is worth mentioning that studies typically focus on the lowest-lying exciton state and rarely address the higher-lying energy levels within this context. This makes it more challenging to rationalize a blueshift of the absorption of the higher-lying energy states. Theoretical work addressing the broad-band optical response of MoS_2 in the presence of excited carriers showed a clear difference between the excitonic response and the higher-energy *C* band absorption. While the excitons engaged in a distinctive competitive behavior between the BGR and BER, the *C* peak was relatively stable against increasing carrier densities and even showed signs of a small blueshift.[57] In this regard, Steinhoff et al.[57] suggest that an interpretation of higher-lying energy states is far from trivial.

Regime II (>3 ps to 1 ns): Redshifts and Linewidth Narrowing. The initial line broadening and blueshift exhibit a cross-over into a peculiar narrowing and redshift on the same timescale as the THz conductivity decreases. Figure 6a shows the TA spectra at a long time delay, indicating a dominant redshift ($\Delta E_{exciton} < 0$, see Figure 6b) that persists up to 1 ns (Figure 6a,b) and scales linearly with the photon flux (see Figure 6c). In addition, such an analysis reveals a dominant linear scaling of the exciton linewidth Δw and the shift of background absorbance ΔE_{bck} with the pump fluence (see Supporting Information Section 8), an observation that again points to a common mechanistic origin. Such a transition from a blueshift to a redshift has been observed in WS_2.[49,55] In these studies, the cross-over was attributed to an initial blueshift due to BER, followed by a redshift due to lattice heating, arising from nonradiative recombination of electrons and holes on longer timescales. On the other hand, as outlined above, a decay of charge carriers due to recombination would also alter the intricate interplay between BER and BGR. Irrespective of whether the redshift is induced by a temperature effect or by a variation in charge carrier density, tipping the balance between BER and BGR, both are due to the recombination of free mobile charge carriers, an interpretation in agreement with the decay of the real THz conductivity signal. In addition, the linear dependence of the exciton shift with the pump fluence points to a trapping mechanism rather than to an Auger-like higher-order recombination mechanism.

As carrier−carrier scattering induces a broadening of the line, carrier loss inevitably reduces the width. While such a process accounts for the decay in broadening, it does not explain the small, albeit measurable, narrowing we observe afterward. A line narrowing might occur due to different mechanisms; nonetheless, they again all reflect nonradiative capture events:

1. Homogenization of the local environment: A line narrowing can be interpreted as a reduction of the inhomogeneous linewidth of the excitonic optical absorption profile, typically due to a homogenization of the environment. Such homogenization could arise from screening of parasitic in-plane electric fields arising

https://doi.org/10.1021/acs.jpcc.1c05268
J. Phys. Chem. C 2021, 125, 20993−21002

from local potentials, *e.g.*, as a result of charged or ionized defects,[58,59] or due to preexisting built-in fields.

We note that such screening of internal electric fields by photogenerated free charges has been studied before by numerous authors on epitaxially grown semiconductor quantum wells.[60−63] The internal electric field in these 2D systems originated from the intrinsic piezoelectric property of the material. Unlike 2H TMDs, such as $MoSe_2$ and WSe_2, ReS_2 crystallizes in a distorted 1T′-$CdCl_2$ lattice-type, similar to WTe_2. Although a ReS_2 monolayer (unit cell) is centrosymmetric, exfoliated multilayered stacks of ReS_2 are known to favor an anisotropic *AB* stacking order where one layer is shifted with respect to the other.[17,18] We, indeed, observed such a stacking order by Raman spectroscopy in our previous work (Supporting Information Section S1).[27] In a similar case, Cobden and co-workers reported the presence of ferroelectricity in bilayer 1T′-WTe_2, while it was absent in a monolayer.[65] This distinctive behavior stemmed from surface dipoles that arise due to the uniquely distorted 1T′-phase. This suggests that an internal field in ReS_2 is not unlikely.

Alternatively, Heinz and co-workers outlined that dielectric disorder is the dominant source of inhomogeneities in 2D materials[66] due to the strong effect on the exciton binding energy. Dielectric disorder originates from local fluctuations of the permittivity, for example, due to localized defects. But either by neutralizing internal or parasitic electric fields or by means of improving dielectric order, charge carrier capture into charged defects will always homogenize the energy landscape, thereby reducing inhomogeneous broadening and eventually narrowing the linewidth of the excitonic optical absorption profile.

2. Interlayer coupling: An alternative interpretation relates to the interlayer coupling in ReS_2. It is well known that interlayer interactions can broaden an exciton profile.[17,64] These effects are subtle, manifesting on changes of the interlayer distance less than 0.1 Å. An excellent example is the existence of two dominant polytypes in ReS_2, labeled as *AB* (anisotropic) and *AA* (isotropic).[17,18] Recently, it has been reported that spectral lines in the *AB* polytype are broader and blue-shifted with respect to AA.[64] These differences relate to the stronger interlayer coupling between stacked ReS_2 layers in the *AB* polytype—the dominant polytype present in the liquid-phase exfoliated ReS_2.[17,27] In this respect, a sudden carrier-capture event would locally polarize/charge the sheet and repel adjacent layers, reduces the interlayer coupling—thereby partially undoing differences between *AB* and *AA*. As a result, the excitonic absorption profile could narrow.

CONCLUSIONS

In summary, we have analyzed the dynamics of photogenerated charge carriers in high-quality exfoliated ReS_2 nanoflakes using time-resolved pump-probe laser spectroscopy with optical and THz conductivity detection. We identified two distinct time regimes of charge carrier dynamics, both of which are dominated by responses due to unbound charge carriers. In the first time regime, free charge carriers induce collisional broadening of the exciton energy and a blueshift due to screening of the electron−hole attraction. In the second time regime, peculiar line narrowing effects are identified, which could be due to charge carriers reducing effects of built-in fields or charged defects. Besides providing a toolbox to gain insights into a series of complex and interplaying optical nonlinearities in commonly used transient absorption spectroscopy of TMD materials, the generation of unbound and mobile charge carriers in such ultrathin materials is equally interesting from a practical point of view, as mobile charges are highly desired in photovoltaic devices or photodetectors.

ASSOCIATED CONTENT

Supporting Information

The Supporting Information is available free of charge at https://pubs.acs.org/doi/10.1021/acs.jpcc.1c05268.

Synthesis/structural characterization of ReS_2 nanoflakes; description of line shape analysis in TA experiments; in-depth discussion of the spectral deconvolution procedure; calculation of the exciton polarizability and scattering length; analysis of the frequency dependence of the THz conductivity using the Drude−Smith model; and fluence-dependent measurement in the light of the lattice heating (PDF)

AUTHOR INFORMATION

Corresponding Author

Pieter Geiregat − *Physics and Chemistry of Nanostructures, Department of Chemistry, Ghent University, Ghent 9000, Belgium; Center for Nano and Biophotonics, Ghent University, Ghent 9000, Belgium;* orcid.org/0000-0001-7217-8738; Email: pieter.geiregat@ugent.be

Authors

Pieter Schiettecatte − *Physics and Chemistry of Nanostructures, Department of Chemistry, Ghent University, Ghent 9000, Belgium; Center for Nano and Biophotonics, Ghent University, Ghent 9000, Belgium*

Deepika Poonia − *Optoelectronic Materials Section, Department of Chemical Engineering, Delft University of Technology, 2629 HZ Delft, The Netherlands*

Ivo Tanghe − *Physics and Chemistry of Nanostructures, Department of Chemistry, Ghent University, Ghent 9000, Belgium; Center for Nano and Biophotonics, Ghent University, Ghent 9000, Belgium*

Sourav Maiti − *Optoelectronic Materials Section, Department of Chemical Engineering, Delft University of Technology, 2629 HZ Delft, The Netherlands;* orcid.org/0000-0003-1983-9159

Michele Failla − *Optoelectronic Materials Section, Department of Chemical Engineering, Delft University of Technology, 2629 HZ Delft, The Netherlands;* orcid.org/0000-0001-5822-8049

Sachin Kinge − *Materials Research & Development, Toyota Motor Europe, B1930 Zaventem, Belgium*

Zeger Hens − *Physics and Chemistry of Nanostructures, Department of Chemistry, Ghent University, Ghent 9000, Belgium; Center for Nano and Biophotonics, Ghent University, Ghent 9000, Belgium;* orcid.org/0000-0002-7041-3375

Laurens D. A. Siebbeles − *Optoelectronic Materials Section, Department of Chemical Engineering, Delft University of*

Technology, 2629 HZ Delft, The Netherlands; orcid.org/0000-0002-4812-7495

Complete contact information is available at: https://pubs.acs.org/10.1021/acs.jpcc.1c05268

Author Contributions

⊥P.S. and D.P. contributed equally to this work.

Author Contributions

P.S. and D.P. contributed equally to this work. Both contributed to the spectroscopy and synthesis, data analysis, and writing of the paper. I.T. wrote the analysis code for the spectral deconvolution. M.F. assisted with the THz measurements. S.M. and Z.H. participated in the discussions. L.D.A.S. and P.G. initiated, supervised the research, and wrote the manuscript.

Notes

The authors declare no competing financial interest.

■ ACKNOWLEDGMENTS

Z.H. acknowledges Ghent University for Research Funding (GOA 01G01019). This research received funding from the Netherlands Organization for Scientific Research (NWO) in the framework of the Materials for sustainability and from the Ministry of Economic Affairs in the framework of the PPP allowance and is also part of the NWO research program TOP-ECHO with project number 715.016.002. P.S. acknowledges the FWO-Vlaanderen for a fellowship (FWO-SB scholarship, FWO project number: 1S40117N). The authors thank Arjan Houtepen, Gianluca Grimaldi, and Indy du Fossé for their assistance with the initial measurements.

■ REFERENCES

(1) Wang, Q. H.; Kalantar-Zadeh, K.; Kis, A.; Coleman, J. N.; Strano, M. S. Electronics and Optoelectronics of Two-Dimensional Transition Metal Dichalcogenides. *Nat. Nanotechnol.* **2012**, *7*, 699−712.

(2) Tongay, S.; Sahin, H.; Ko, C.; Luce, A.; Fan, W.; Liu, K.; Zhou, J.; Huang, Y.-S.; Ho, C.-H.; Yan, J.; et al. Monolayer Behaviour in Bulk ReS_2 Due to Electronic and Vibrational Decoupling. *Nat. Commun.* **2014**, *5*, No. 3252.

(3) Rahman, M.; Davey, K.; Qiao, S.-Z. Advent of 2D Rhenium Disulfide (ReS_2): Fundamentals to Applications. *Adv. Funct. Mater.* **2017**, *27*, No. 1606129.

(4) Dileep, K.; Sahu, R.; Sarkar, S.; Peter, S. C.; Datta, R. Layer Specific Optical Band Gap Measurement at Nanoscale in MoS_2 and ReS_2 van Der Waals Compounds by High Resolution Electron Energy Loss Spectroscopy. *J. Appl. Phys.* **2016**, *119*, No. 114309.

(5) Liu, E.; Fu, Y.; Wang, Y.; Feng, Y.; Liu, H.; Wan, X.; Zhou, W.; Wang, B.; Shao, L.; Ho, C.-H.; et al. Integrated Digital Inverters Based on Two-Dimensional Anisotropic ReS_2 Field-Effect Transistors. *Nat. Commun.* **2015**, *6*, No. 6991.

(6) Echeverry, J. P.; Gerber, I. C. Theoretical Investigations of the Anisotropic Optical Properties of Distorted 1 T ReS_2 and $ReSe_2$ Monolayers, Bilayers, and in the Bulk Limit. *Phys. Rev. B* **2018**, *97*, No. 075123.

(7) Xu, K.; Deng, H.-X.; Wang, Z.; Huang, Y.; Wang, F.; Li, S.-S.; Luo, J.-W.; He, J. Sulfur Vacancy Activated Field Effect Transistors Based on ReS_2 Nanosheets. *Nanoscale* **2015**, *7*, 15757−15762.

(8) Liu, F.; Zheng, S.; He, X.; Chaturvedi, A.; He, J.; Chow, W. L.; Mion, T. R.; Wang, X.; Zhou, J.; Fu, Q.; et al. Highly Sensitive Detection of Polarized Light Using Anisotropic 2D ReS_2. *Adv. Funct. Mater.* **2016**, *26*, 1169−1177.

(9) Liao, W.; Wei, W.; Tong, Y.; Chim, W. K.; Zhu, C. Low-Frequency Noise in Layered ReS_2 Field Effect Transistors on HfO_2 and Its Application for PH Sensing. *ACS Appl. Mater. Interfaces* **2018**, *10*, 7248−7255.

(10) Shim, J.; Oh, A.; Kang, D.-H.; Oh, S.; Jang, S. K.; Jeon, J.; Jeon, M. H.; Kim, M.; Choi, C.; Lee, J.; et al. High-Performance 2D Rhenium Disulfide (ReS_2) Transistors and Photodetectors by Oxygen Plasma Treatment. *Adv. Mater.* **2016**, *28*, 6985−6992.

(11) Hafeez, M.; Gan, L.; Li, H.; Ma, Y.; Zhai, T. Large-Area Bilayer ReS_2 Film/Multilayer ReS_2 Flakes Synthesized by Chemical Vapor Deposition for High Performance Photodetectors. *Adv. Funct. Mater.* **2016**, *26*, 4551−4560.

(12) Hafeez, M.; Gan, L.; Li, H.; Ma, Y.; Zhai, T. Chemical Vapor Deposition Synthesis of Ultrathin Hexagonal $ReSe_2$ Flakes for Anisotropic Raman Property and Optoelectronic Application. *Adv. Mater.* **2016**, *28*, 8296−8301.

(13) Wang, J.; Zhou, Y. J.; Xiang, D.; Ng, S. J.; Watanabe, K.; Taniguchi, T.; Eda, G. Polarized Light-Emitting Diodes Based on Anisotropic Excitons in Few-Layer ReS_2. *Adv. Mater.* **2020**, *32*, No. 2001890.

(14) Yang, A.; Gao, J.; Li, B.; Tan, J.; Xiang, Y.; Gupta, T.; Li, L.; Suresh, S.; Idrobo, J. C.; Lu, T.-M.; et al. Humidity Sensing Using Vertically Oriented Arrays of ReS_2 Nanosheets Deposited on an Interdigitated Gold Electrode. *2D Mater.* **2016**, *3*, No. 045012.

(15) Chenet, D. A.; Aslan, O. B.; Huang, P. Y.; Fan, C.; van der Zande, A. M.; Heinz, T. F.; Hone, J. C. In-Plane Anisotropy in Mono- and Few-Layer ReS_2 Probed by Raman Spectroscopy and Scanning Transmission Electron Microscopy. *Nano Lett.* **2015**, *15*, 5667−5672.

(16) Wang, R.; Xu, X.; Yu, Y.; Ran, M.; Zhang, Q.; Li, A.; Zhuge, F.; Li, H.; Gan, L.; Zhai, T. The Mechanism of the Modulation of Electronic Anisotropy in Two-Dimensional ReS_2. *Nanoscale* **2020**, *12*, 8915−8921.

(17) Qiao, X.-F.; Wu, J.-B.; Zhou, L.; Qiao, J.; Shi, W.; Chen, T.; Zhang, X.; Zhang, J.; Ji, W.; Tan, P.-H. Polytypism and Unexpected Strong Interlayer Coupling in Two-Dimensional Layered ReS_2. *Nanoscale* **2016**, *8*, 8324−8332.

(18) Hart, L.; Dale, S.; Hoye, S.; Webb, J. L.; Wolverson, D. Rhenium Dichalcogenides: Layered Semiconductors with Two Vertical Orientations. *Nano Lett.* **2016**, *16*, 1381−1386.

(19) Cui, Q.; He, J.; Bellus, M. Z.; Mirzokarimov, M.; Hofmann, T.; Chiu, H.-Y.; Antonik, M.; He, D.; Wang, Y.; Zhao, H. Transient Absorption Measurements on Anisotropic Monolayer ReS_2. *Small* **2015**, *11*, 5565−5571.

(20) Fujita, T.; Ito, Y.; Tan, Y.; Yamaguchi, H.; Hojo, D.; Hirata, A.; Voiry, D.; Chhowalla, M.; Chen, M. Chemically Exfoliated ReS_2 Nanosheets. *Nanoscale* **2014**, *6*, 12458−12462.

(21) Al-Dulaimi, N.; Lewis, E. A.; Lewis, D. J.; Howell, S. K.; Haigh, S. J.; O'Brien, P. Sequential Bottom-up and Top-down Processing for the Synthesis of Transition Metal Dichalcogenide Nanosheets: The Case of Rhenium Disulfide (ReS_2). *Chem. Commun.* **2016**, *52*, 7878−7881.

(22) Keyshar, K.; Gong, Y.; Ye, G.; Brunetto, G.; Zhou, W.; Cole, D. P.; Hackenberg, K.; He, Y.; Machado, L.; Kabbani, M.; et al. Chemical Vapor Deposition of Monolayer Rhenium Disulfide (ReS_2). *Adv. Mater.* **2015**, *27*, 4640−4648.

(23) Martín-García, B.; Spirito, D.; Bellani, S.; Prato, M.; Romano, V.; Polovitsyn, A.; Brescia, R.; Oropesa-Nuñez, R.; Najafi, L.; Ansaldo, A.; et al. Extending the Colloidal Transition Metal Dichalcogenide Library to ReS_2 Nanosheets for Application in Gas Sensing and Electrocatalysis. *Small* **2019**, *15*, No. 1904670.

(24) Schiettecatte, P.; Geiregat, P.; Hens, Z. Ultrafast Carrier Dynamics in Few-Layer Colloidal Molybdenum Disulfide Probed by Broadband Transient Absorption Spectroscopy. *J. Phys. Chem. C* **2019**, *123*, 10571−10577.

(25) Zhou, P.; Tanghe, I.; Schiettecatte, P.; van Thourhout, D.; Hens, Z.; Geiregat, P. Ultrafast Carrier Dynamics in Colloidal WS_2 Nanosheets Obtained through a Hot Injection Synthesis. *J. Chem. Phys.* **2019**, *151*, No. 164701.

(26) Coleman, J. N. Liquid Exfoliation of Defect-Free Graphene. *Acc. Chem. Res.* **2013**, *46*, 14−22.

(27) Schiettecatte, P.; Rousaki, A.; Vandenabeele, P.; Geiregat, P.; Hens, Z. Liquid-Phase Exfoliation of Rhenium Disulfide by Solubility Parameter Matching. *Langmuir* **2020**, *36*, 15493−15500.
(28) Maiti, S.; Poonia, D.; Schiettecatte, P.; Hens, Z.; Geiregat, P.; Kinge, S.; Siebbeles, L. D. A. Generating Triplets in Organic Semiconductor Tetracene upon Photoexcitation of Transition Metal Dichalcogenide ReS_2. *J. Phys. Chem. Lett.* **2021**, *12*, 5256−5260.
(29) Jawaid, A.; Nepal, D.; Park, K.; Jespersen, M.; Qualley, A.; Mirau, P.; Drummy, L. F.; Vaia, R. A. Mechanism for Liquid Phase Exfoliation of MoS_2. *Chem. Mater.* **2016**, *28*, 337−348.
(30) Backes, C.; Higgins, T. M.; Kelly, A.; Boland, C.; Harvey, A.; Hanlon, D.; Coleman, J. N. Guidelines for Exfoliation, Characterization and Processing of Layered Materials Produced by Liquid Exfoliation. *Chem. Mater.* **2017**, *29*, 243−255.
(31) Spoor, F. C. M.; Kunneman, L. T.; Evers, W. H.; Renaud, N.; Grozema, F. C.; Houtepen, A. J.; Siebbeles, L. D. A. Hole Cooling Is Much Faster than Electron Cooling in PbSe Quantum Dots. *ACS Nano* **2016**, *10*, 695−703.
(32) Spoor, F. C. M.; Tomić, S.; Houtepen, A. J.; Siebbeles, L. D. A. Broadband Cooling Spectra of Hot Electrons and Holes in PbSe Quantum Dots. *ACS Nano* **2017**, *11*, 6286−6294.
(33) Lauth, J.; Kulkarni, A.; Spoor, F. C. M.; Renaud, N.; Grozema, F. C.; Houtepen, A. J.; Schins, J. M.; Kinge, S.; Siebbeles, L. D. A. Photogeneration and Mobility of Charge Carriers in Atomically Thin Colloidal InSe Nanosheets Probed by Ultrafast Terahertz Spectroscopy. *J. Phys. Chem. Lett.* **2016**, *7*, 4191−4196.
(34) Grimaldi, G.; Geuchies, J. J.; van der Stam, W.; du Fossé, I.; Brynjarsson, B.; Kirkwood, N.; Kinge, S.; Siebbeles, L. D. A.; Houtepen, A. J. Spectroscopic Evidence for the Contribution of Holes to the Bleach of Cd-Chalcogenide Quantum Dots. *Nano Lett.* **2019**, *19*, 3002−3010.
(35) Kunneman, L. T.; Zanella, M.; Manna, L.; Siebbeles, L. D. A.; Schins, J. M. Mobility and Spatial Distribution of Photoexcited Electrons in CdSe/CdS Nanorods. *J. Phys. Chem. C* **2013**, *117*, 3146−3151.
(36) Evers, W. H.; Schins, J. M.; Aerts, M.; Kulkarni, A.; Capiod, P.; Berthe, M.; Grandidier, B.; Delerue, C.; van der Zant, H. S. J.; van Overbeek, C.; Peters, J. L.; et al. High Charge Mobility in Two-Dimensional Percolative Networks of PbSe Quantum Dots Connected by Atomic Bonds. *Nat. Commun.* **2015**, *6*, No. 8195.
(37) Lauth, J.; Failla, M.; Klein, E.; Klinke, C.; Kinge, S.; Siebbeles, L. D. A. Photoexcitation of PbS Nanosheets Leads to Highly Mobile Charge Carriers and Stable Excitons. *Nanoscale* **2019**, *11*, 21569−21576.
(38) Jadczak, J.; Kutrowska-Girzycka, J.; Smoleński, T.; Kossacki, P.; Huang, Y. S.; Bryja, L. Exciton Binding Energy and Hydrogenic Rydberg Series in Layered ReS_2. *Sci. Rep.* **2019**, *9*, No. 1578.
(39) Ulbricht, R.; Hendry, E.; Shan, J.; Heinz, T. F.; Bonn, M. Carrier Dynamics in Semiconductors Studied with Time-Resolved Terahertz Spectroscopy. *Rev. Mod. Phys.* **2011**, *83*, 543−586.
(40) Lloyd-Hughes, J.; Jeon, T.-I. A Review of the Terahertz Conductivity of Bulk and Nano-Materials. *J. Infrared, Millimeter, Terahertz Waves* **2012**, *33*, 871−925.
(41) Yu, Z. G.; Cai, Y.; Zhang, Y.-W. Robust Direct Bandgap Characteristics of One- and Two-Dimensional ReS_2. *Sci. Rep.* **2015**, *5*, No. 13783.
(42) Tiong, K. K.; Ho, C. H.; Huang, Y. S. The Electrical Transport Properties of ReS_2 and $ReSe_2$ Layered Crystals. *Solid State Commun.* **1999**, *111*, 635−640.
(43) Liu, E.; Long, M.; Zeng, J.; Luo, W.; Wang, Y.; Pan, Y.; Zhou, W.; Wang, B.; Hu, W.; Ni, Z.; et al. High Responsivity Phototransistors Based on Few-Layer ReS_2 for Weak Signal Detection. *Adv. Funct. Mater.* **2016**, *26*, 1938−1944.
(44) Cunningham, P. D.; McCreary, K. M.; Hanbicki, A. T.; Currie, M.; Jonker, B. T.; Hayden, L. M. Charge Trapping and Exciton Dynamics in Large-Area CVD Grown MoS_2. *J. Phys. Chem. C* **2016**, *120*, 5819−5826.
(45) Hindmarsh, W. R.; Petford, A. D.; Smith, G.; Kuhn, H. G. Interpretation of Collision Broadening and Shift in Atomic Spectra. *Proc. R. Soc. London, Ser. A* **1967**, *297*, 296−304.
(46) Leite, R. C. C.; Shah, J.; Gordon, J. P. Effect of Electron-Exciton Collisions on the Free-Exciton Linewidth in Epitaxial GaAs. *Phys. Rev. Lett.* **1969**, *23*, 1332−1335.
(47) Schultheis, L.; Kuhl, J.; Honold, A.; Tu, C. W. Ultrafast Phase Relaxation of Excitons via Exciton-Exciton and Exciton-Electron Collisions. *Phys. Rev. Lett.* **1986**, *57*, 1635−1638.
(48) Sim, S.; Park, J.; Song, J.-G.; In, C.; Lee, Y.-S.; Kim, H.; Choi, H. Exciton Dynamics in Atomically Thin MoS_2: Interexcitonic Interaction and Broadening Kinetics. *Phys. Rev. B* **2013**, *88*, No. 075434.
(49) Cunningham, P. D.; Hanbicki, A. T.; McCreary, K. M.; Jonker, B. T. Photoinduced Bandgap Renormalization and Exciton Binding Energy Reduction in WS_2. *ACS Nano* **2017**, *11*, 12601−12608.
(50) Wang, G.; Chernikov, A.; Glazov, M. M.; Heinz, T. F.; Marie, X.; Amand, T.; Urbaszek, B. Colloquium: Excitons in Atomically Thin Transition Metal Dichalcogenides. *Rev. Mod. Phys.* **2018**, *90*, No. 021001.
(51) Schmitt-Rink, S.; Ell, C.; Haug, H. Many-Body Effects in the Absorption, Gain, and Luminescence Spectra of Semiconductor Quantum-Well Structures. *Phys. Rev. B* **1986**, *33*, 1183−1189.
(52) Schmitt-Rink, S.; Chemla, D. S.; Miller, D. A. B. Linear and Nonlinear Optical Properties of Semiconductor Quantum Wells. *Adv. Phys.* **1989**, *38*, 89−188.
(53) Wake, D. R.; Yoon, H. W.; Wolfe, J. P.; Morkoç, H. Response of Excitonic Absorption Spectra to Photoexcited Carriers in GaAs Quantum Wells. *Phys. Rev. B* **1992**, *46*, 13452−13460.
(54) Hulin, D.; Mysyrowicz, A.; Antonetti, A.; Migus, A.; Masselink, W. T.; Morkoç, H.; Gibbs, H. M.; Peyghambarian, N. Well-Size Dependence of Exciton Blue Shift in GaAs Multiple-Quantum-Well Structures. *Phys. Rev. B* **1986**, *33*, 4389−4391.
(55) Ruppert, C.; Chernikov, A.; Hill, H. M.; Rigosi, A. F.; Heinz, T. F. The Role of Electronic and Phononic Excitation in the Optical Response of Monolayer WS_2 after Ultrafast Excitation. *Nano Lett.* **2017**, *17*, 644−651.
(56) Wu, X.; Trinh, M. T.; Zhu, X.-Y. Excitonic Many-Body Interactions in Two-Dimensional Lead Iodide Perovskite Quantum Wells. *J. Phys. Chem. C* **2015**, *119*, 14714−14721.
(57) Steinhoff, A.; Rösner, M.; Jahnke, F.; Wehling, T. O.; Gies, C. Influence of Excited Carriers on the Optical and Electronic Properties of MoS_2. *Nano Lett.* **2014**, *14*, 3743−3748.
(58) Moody, G.; Kavir Dass, C.; Hao, K.; Chen, C.-H.; Li, L.-J.; Singh, A.; Tran, K.; Clark, G.; Xu, X.; Berghäuser, G.; et al. Intrinsic Homogeneous Linewidth and Broadening Mechanisms of Excitons in Monolayer Transition Metal Dichalcogenides. *Nat. Commun.* **2015**, *6*, No. 8315.
(59) Stoneham, A. M. Shapes of Inhomogeneously Broadened Resonance Lines in Solids. *Rev. Mod. Phys.* **1969**, *41*, 82−108.
(60) Wood, T. H.; Burrus, C. A.; Miller, D. A. B.; Chemla, D. S.; Damen, T. C.; Gossard, A. C.; Wiegmann, W. High-speed Optical Modulation with GaAs/GaAlAs Quantum Wells in a P-i-n Diode Structure. *Appl. Phys. Lett.* **1984**, *44*, 16−18.
(61) Miller, D. A. B.; Chemla, D. S.; Damen, T. C.; Gossard, A. C.; Wiegmann, W.; Wood, T. H.; Burrus, C. A. Electric Field Dependence of Optical Absorption near the Band Gap of Quantum-Well Structures. *Phys. Rev. B* **1985**, *32*, 1043−1060.
(62) Weiner, J. S.; Miller, D. A. B.; Chemla, D. S.; Damen, T. C.; Burrus, C. A.; Wood, T. H.; Gossard, A. C.; Wiegmann, W. Strong Polarization-sensitive Electroabsorption in GaAs/AlGaAs Quantum Well Waveguides. *Appl. Phys. Lett.* **1985**, *47*, 1148−1150.
(63) Kuo, Y.-H.; Lee, Y. K.; Ge, Y.; Ren, S.; Roth, J. E.; Kamins, T. I.; Miller, D. A. B.; Harris, J. S. Strong Quantum-Confined Stark Effect in Germanium Quantum-Well Structures on Silicon. *Nature* **2005**, *437*, 1334−1336.
(64) Zhou, Y.; Maity, N.; Rai, A.; Juneja, R.; Meng, X.; Roy, A.; Zhang, Y.; Xu, X.; Lin, J.-F.; Banerjee, S. K.; et al. Stacking-Order-

Driven Optical Properties and Carrier Dynamics in ReS_2. *Adv. Mater.* **2020**, *32*, No. 1908311.
(65) Fei, Z.; Zhao, W.; Palomaki, T. A.; Sun, B.; Miller, M. K.; Zhao, Z.; Yan, J.; Xu, X.; Cobden, D. H. Ferroelectric Switching of a Two-Dimensional Metal. *Nature* **2018**, *560*, 336−339.
(66) Raja, A.; Waldecker, L.; Zipfel, J.; Cho, Y.; Brem, S.; Ziegler, J. D.; Kulig, M.; Taniguchi, T.; Watanabe, K.; Malic, E.; et al. A. Dielectric Disorder in Two-Dimensional Materials. *Nat. Nanotechnol.* **2019**, *14*, 832−837.

https://doi.org/10.1021/acs.jpcc.1c05268
J. Phys. Chem. C 2021, 125, 20993−21002